Research
A SCIENCE PARTNER JOURNAL

RESEARCH ARTICLE

Continuous Multi-Material Additive Manufacturing

Jiawei Sun[1,2†], Wangjun Xiong[1,2†], Lidian Zhang[3], Xuan Guo[4], Yanlin Song[1,2*], and Lei Wu[1,2*]

[1]Key Laboratory of Green Printing, Institute of Chemistry, Chinese Academy of Sciences, Beijing 100190, P. R. China. [2]University of Chinese Academy of Sciences, Beijing 100049, P. R. China. [3]China National Petroleum & Chemical Planning Institute, Beijing 100013, P. R. China. [4]CAS Key Laboratory of Bio-inspired Materials and Interfacial Sciences, Technical Institute of Physics and Chemistry, Chinese Academy of Sciences, Beijing 100190, P. R. China.

*Address correspondence to: wulei1989@iccas.ac.cn (L.W.); ylsong@iccas.ac.cn (Y.S.)
†These authors contributed equally to this work.

Citation: Sun J, Xiong W, Zhang L, Guo X, Song Y, Wu L. Continuous Multi-Material Additive Manufacturing. *Research* 2025;8:Article 0889. https://doi.org/10.34133/research.0889

Submitted 11 July 2025
Revised 13 August 2025
Accepted 19 August 2025
Published 18 September 2025

Copyright © 2025 Jiawei Sun et al. Exclusive licensee Science and Technology Review Publishing House. No claim to original U.S. Government Works. Distributed under a Creative Commons Attribution License (CC BY 4.0).

Slice-based additive manufacturing has been intensively investigated due to its potential in complex 3-dimensional (3D) structure construction across various fields. Current researches focus on curing surface and resin formation regulation to realize continuous printing. However, multi-material construction necessitates vat switching, compromising construction continuity. Achieving simultaneous multi-material construction within a single layer and enabling continuous multi-material construction continue to pose substantial challenges. Here, we present a continuous multi-material additive manufacturing (CMAM) approach by integrating extruding multi-liquid phases into droplet-based 3D printing system. The multi-droplet-based multi-liquid reservoir enables both 2D patterning of multi-liquid materials and their real-time curing, along with continuous resin replenishment to achieve continuous multi-material 3D construction. Additionally, extrusion parameters (extrusion number, spatial distribution, and extrusion flow rates) are controllable layer by layer, leading to controllable muti-material 3D distribution. Interfacial fusion can be controlled by adjusting printing speed and resin viscosity, leading to enhanced mechanical adhesions of 2 materials without influencing interfacial boundary precision. Increasing extrusion number can realize multi-material 3D structure construction with controlled material distribution, which can be extended to 3D structure-based anti-counterfeiting and soft robotics, guaranteeing a highly efficient and sustainable approach to multi-material 3D fabrication.

Introduction

Additive manufacturing, which is also well known as 3-dimensional (3D) printing, is a sustainable fabrication approach that has evolved into a powerful platform for 3D structure construction due to its design freedom, ease of operation, and mold-free processing [1–3]. Its applications span structural materials [4–7], sensors, devices [8–12], soft robotics [13–17], and tissue engineering [18–22]. Notably, among various 3D printing techniques, digital light processing stands out by projecting full-layer ultraviolet (UV) patterns, which enables high-speed production for instantaneous photopolymerization. Since the voxel-to-slice conversion step is skipped, the manufacturing process becomes faster [23–26]. A typical 3D printing setup consists of 3 primary components: (a) a UV light source that projects sliced layer patterns, (b) a resin container serving both as a reservoir for liquid photopolymer and as the curing surface for UV-induced polymerization, and (c) a moving platform with an attached supporting plate where the 3D structure is progressively fabricated. The UV polymerization process of liquid resin at the curing surface to form cured structure is the basic process to prepare one slice. Recent studies have demonstrated that optimizing the fabrication process through interfacial engineering can improve both manufacturing efficiency and product quality [27]. Specifically, the introduction of a dynamic, liquid-like separation layer between the curing interface and printed structure minimizes interfacial adhesion forces, facilitating continuous fabrication while maintaining dimensional accuracy [28,29]. The inert "liquid-like" separation layer can be realized through various approaches based on curing surface modification, including the "dead zone" mechanism in the continuous liquid interface production technology [30], low-adhesive "slippery curing surfaces" [31], and the "flowing immiscible fluorinated oil with cooling systems" in the high-area rapid printing technology [32], or advanced resin formulations [33–35] employing multiple photoinitiators matched with corresponding multiple UV light. Beyond conventional interface regulation, construction control can be attained by increasing or decreasing the involved interfaces. The establishment of a 3-phase contact line (TCL) [36] facilitates droplet-based manufacturing with superior material utilization, achieved through precise manipulation of the receding TCL. Rotational slicing about the symmetric

axis (versus conventional z-axis motion) enables curing surface-independent volumetric manufacturing. Furthermore, integrating extra microfluidic [37], electric [38,39], and magnetic [40] control systems at curing interfaces allows precise modulation of resin properties and material composition during printing.

However, there exists a fundamental trade-off between construction continuity and simultaneous multi-material deposition. State-of-the-art multi-material 3D printing employs sequential resin exchange in the printing vat to change the resin employed for the current layer [41–46]. The vat switching procedure necessitates interruption of ongoing layer polymerization, thereby preventing continuous multi-material deposition within individual layers [47,48]. While deposition-based techniques like direct ink writing (DIW) [49,50] and inkjet 3D printing [51] can achieve continuous multi-material fabrication through multi-nozzle systems with dynamic material switching of nozzles [52,53], their voxel-by-voxel deposition mechanism necessitates sequential x–y plane patterning followed by z-axis stacking. These approaches result in comparatively slower build rates and reduced resolution relative to photopolymerization methods (Table S1), making continuous slice-based multi-material polymerization an unresolved challenge.

Herein, we present CMAM approach that utilizes patterned slices as the fundamental molding unit. Drawing inspiration from the on-demand fabrication capabilities of extrusion-based 3D printing technique [54] and one-droplet 3D printing methodology [55], we introduce controlled number and distribution of extrusion devices at the curing surface. Based on the retractable TCL endowed by the droplet reservoir, multi-liquid can be patterned inside the reservoir through continuous extrusion. With continuous UV curing depleting the liquid resin extrusion, droplet-based 3D printing enables simultaneous multi-material extrusion and curing in a continuous process. By precisely controlling resin extrusion parameters (rate, volume, and spatial distribution), this approach can fabricate controllable planar-to-3D interfaces with 4 or more materials simultaneously in a single layer and finally enables a continuous multi-material construction process. With liquid phase contact and simultaneous UV polymerization, interfacial mechanical performance was enhanced through interfacial fusion while maintaining sharply defined 3D structural boundaries. Leveraging precise control over material composition and spatial distribution, this method enables single-layer-based multi-material fabrication and further the complex multi-material structures. These include 3D anti-counterfeiting features with customized material patterns and magnetic-responsive fish constructs with programmed movement trajectories. The system's advantages of uninterrupted multi-material construction and scalable droplet-based build volume expand the range of achievable materials, geometries, and practical applications in additive manufacturing.

Results

CMAM conception and configuration

Figure 1A shows the schematic CMAM system, consisting of 2 key components: (a) a bottom-up continuous manufacturing module for instantaneous slice curing, stacking, and structure fabrication [31], and (b) an extrusion-based resin delivery system that maintains droplet-based material reservoirs while providing real-time resin replenishment. Notably, the self-built bottom-up apparatus features a programmable motion stage with a supporting plate, a UV-transparent curing interface, and a digital UV projector. Scaling to larger construction areas can be accomplished either by deploying multiple x–y plane UV projectors or by scanning a single projector, which will compromise the printing continuity. The extrusion device is also self-built, which is composed of a disposable infusion tube attached through a syringe mounting on a pump. The resin delivery tubes should be positioned exclusively at the TCL, taking care to remain outside the UV projection zone. This placement strategy prevents tube curing while maintaining consistent material delivery during the printing process.

The process begins with the precise deposition of multi-material patterned droplet onto the curing surface, achieved through controlled extrusion parameters (extrusion number, spatial distribution, and extrusion flow rates) that faithfully reproduce the digital spatial material design (step I). Then, the supporting plate moves downward to contact the curing surface with certain thickness of liquid resin in step II. Then, patterned layers are UV cured as the support plate ascends, synchronized with the droplet reservoir's TCL receding (step III) [56]. By continuously replenishing diverse liquid resins into the droplet reservoir according to design, 3D structure with multi-material 3D distribution can be printed with high structural precision, stability, and material efficiency (step IV).

Figure 1B demonstrates the continuous printing process of an Eiffel Tower with 4 different colors, achieved using 4-side extrusion resin delivery tubes operating at identical, real-time-adjusted extrusion rates as Fig. S1 that vary with slice area, resulting in 4 linear interfaces and uniform color distribution (Fig. 1C). The resin delivery tubes should be positioned exclusively at the TCL when the printed patterns become smaller. The distribution of the 4 used materials is confirmed by the optical images captured from multiple capturing angles listed in Fig. 1D. In addition, by regulating corresponding extrusion parameters (extrusion number, spatial distribution, and extrusion flow rates), CMAM with sharp interfacial boundaries is capable, allowing the creation of structurally identical objects with varying internal material arrangements. In detail, it is capable to print 2-material gyroid structures featuring both planar and curved interfaces, and multi-material gyroid structures with controlled material distributions in both the x–y plane and z direction, as shown in Fig. 1E, representing a substantial advancement in additive manufacturing's design space and functional capabilities.

Continuous bimaterial construction

The capability and property of continuous construction of 2 materials are first investigated [57–61]. Figure 2A presents the bilateral extrusion method for creating lamellar structures featuring programmable linear and curved zigzag interfaces. Two commercial liquid resins, which are dyed blue and orange, are extruded simultaneously in the experiment. Their extrusion flow rates are dynamically adjusted timely, ensuring that the combined extrusion rate matches the resin consumption required for layer curing. When equal extrusion rates are maintained, this process yields lamellar structures with perfectly vertical interfaces, as displayed in Fig. 2B (I). By systematically varying the relative extrusion flow rates over time, interface morphology can be precisely controlled, producing tilted linear interfaces (Fig. 2B, II) and zigzag patterns with tunable amplitude and frequency (Fig. 2B, III to VII, and Movie S1). As detailed in Fig. 2B (I to VIII), the left panels display time-dependent extrusion

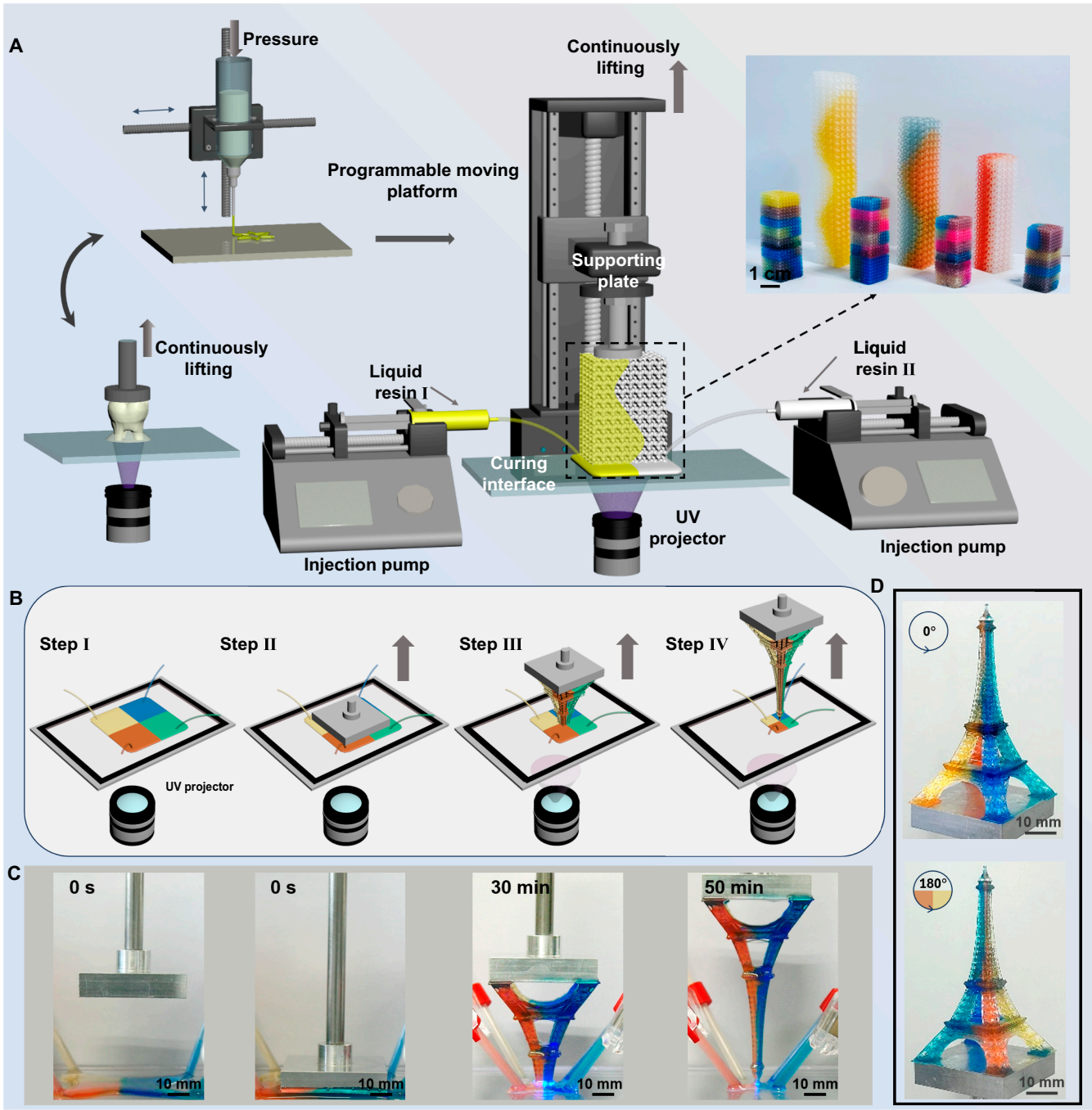


Fig. 1. Schematic configuration of CMAM system. (A) Schematic demonstration of the CMAM system. (B and C) Scheme (B) and time-lapse (C) images of the 4-material Eiffel Tower structure construction process by the CMAM approach. (D) Multi-angle optical microscopy images of the fabricated Eiffel Tower microstructure. (E) Optical images of the examples of multi-material 3D structures printed by this strategy.

profiles for each material, with orange and blue curves corresponding to the respective dyed resins (quantitative parameters provided in Table S2). Optical images (right) show printed lamellar structures with controlled linear, tilted, and zigzag interfaces, fabricated using the extrusion profiles illustrated at the left. Using Fig. 2B (V) as an example, the initial extrusion rates of the orange and blue resins are equal (15 μl/min), positioning the interface at the center of the lamellar structure. As the supporting plate continuously ascends, the extrusion rate of the orange resin linearly increased to 30 μl/min, while that of the blue resin decreased to 0 μl/min over 2.5 min, forming interface A (right side of Fig. 2B, V). Subsequently, the orange resin's extrusion rate linearly dropped to 0 μl/min and the blue resin's rate rise to 30 μl/min over 5 min, producing interface B (right side of Fig. 2B, V). By further following the regulation curve (left side of Fig. 2B, I to VIII), various zigzag interfaces can be fabricated. This demonstrates that CMAM system enables precise spatiotemporal control over material deposition and solidification in planar dimensions. The building slice of 2D multi-material patterned liquid can thus allow simultaneous control of interfacial material distribution and continuous construction.

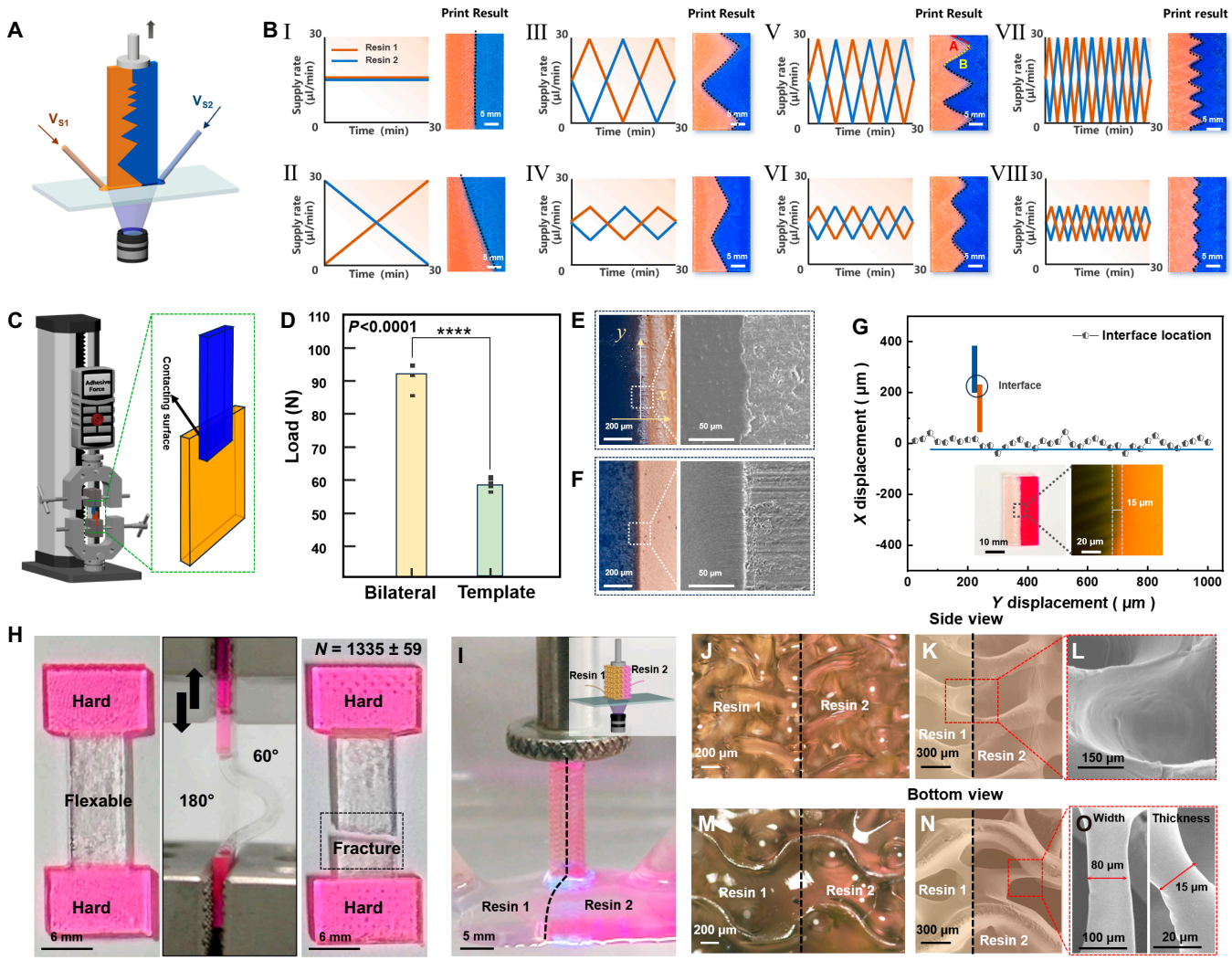


Fig. 2. Bilaterally extruded printing of 2 materials and interfacial analysis. (A) Fabrication scheme for 2-material lamellar structures. (B) Time-dependent extrusion rate modulation and resulting 2-material lamellar structures produced at 20 μm/s supporting plate lifting rate. Eight characteristic interface geometries (I to VIII) illustrate the programmable control range. Representative examples (groups I to VIII) demonstrate the range of achievable architectures. (C) Test scheme for interfacial mechanical performance of bimaterial samples. Blue part is commercial Castable Wax 40 Resin, Formlabs; orange part is commercial Clear Resin, Formlabs dyed orange. (D) Statistical significance of the fracture force extracted of samples prepared from bilateral extrusion and template replication approach. (E) Optical and SEM characterization of the sample interface prepared by bilateral extrusion approach. (F) Optical and SEM characterization of the sample interface prepared by template replication approach. (G) Microstructural interface profile observed in the *x*–*y* plane of (E) the bilateral extrusion-printed lamellar structure. Insets show schematic and fluorescence micrographs of the interface formed between Clear and Elastic resins via bilateral extrusion. (H) Long-term cyclic mechanical characterization of the Hard–Flexible–Hard structure (pink: Hard, Clear with pink dye; transparent: Flexible, Elastic). (I) Optical capture of the downsized 2-material gyroid structure construction configuration; inset is the corresponding scheme. (J) Microscopic image of the area around side interface. (K) SEM image of the area around side interface. (L) SEM image of the enlarged part of (K). (M) Microscopic image of the area around bottom interface. (N) SEM image of the area around bottom interface. (O) SEM image of the enlarged part of (N) from the side view (left) and the top view (right).

The interfacial mechanical behavior of multi-material structures produced via bilateral extrusion printing was investigated through tensile tests aligned with the interface, as displayed in Fig. 2C. The test specimens consisted of 2-lamellar structures with defined contact areas (Fig. 2C, inset), where each material's edges were clamped to the force sensor. A template-replicated sample (Fig. S2) is prepared and served as the control for comparison. During tensile test as shown in Movie S2, the bilaterally extruded samples fractured at the single-material structural side, whereas the control samples failed at the interface. Both the force–displacement profile (Fig. 2D) and fracture force statistics (Fig. S2C) confirm superior interfacial strength in bilaterally extruded samples. Further, optical and scanning electron microscopy (SEM) analyses demonstrate rougher interfacial morphology in bilaterally extruded samples (Fig. 2E) versus template-replicated ones (Fig. 2F). The SEM images profiling of the interfacial transition zone (Fig. 2G) demonstrates that mechanical property enhancement correlates with a ~100-μm-wide fusion zone of 2 materials, where partial polymerization of both resins creates a graded interphase with superior adhesion properties. Then, it is experimentally found that the fusion width is affected by the viscosity difference between the 2 extruded resins. By testing 4 commercial resins including Clear, Grey, Wax, and Elastic (Formlabs, USA) with viscosities of ~1,049, ~1,875, ~2,003, and ~3,914 mPa·s, respectively, 6 distinct 2-material interfaces were successfully printed (Table S3). In single-material extrusion, higher resin viscosity requires greater driving force, typically achieved by increasing the

extrusion rate. The observed fusion width is comparable to that of existing discontinuous and continuous multi-material 3D printing approaches [41,49]. Remarkably, the continuous extrusion strategy enhances interfacial adhesion without compromising printing precision (Table S1), overcoming the traditional trade-off between interfacial strength and dimensional fidelity in multi-material construction.

Furthermore, increasing the viscosity difference between the 2 liquid resins results in a narrower fusion width. The smallest achievable fusion width is ~15 μm, observed between Clear and Elastic resins, which have the largest viscosity difference, as shown in the confocal fluorescence image (Fig. 2G, inset). To evaluate long-term interfacial mechanical performance, we designed and printed a Hard–Flexible–Hard structure with interfaces parallel to the curing surface, leveraging interfacial fusion for enhanced mechanical properties. Notably, the fusion width (~100 μm) in this configuration is larger than in vertically oriented interfaces formed with the same materials. This difference likely arises from incomplete consumption of the Hard resin and rapid replenishment of the Flexible resin for ensuring a continuous liquid layer. Cyclic bending tests (0.2 Hz, 60° to 180° range; Fig. 2H and Fig. S3) demonstrate that the structure can withstand 1,335 ± 59 cycles ($n = 5$) before fracturing in the flexible middle section rather than at the interface, confirming robust interfacial durability and long-term mechanical stability of the multi-material extrusion method.

Then, construction stability is evaluated through comparative analysis between conventional single-material vat photopolymerization and the proposed bilateral multi-material extrusion process. In conventional continuous vat photopolymerization, structural adhesion to the curing interface occurs after prolonged fabrication periods, ultimately resulting in print failure (Fig. S4). In contrast, the continuous bilateral extrusion approach enables fabrication of much taller structures without interfacial adhesion or print failure, which is finally limited only by the maximum travel of the moving platform. This capability permits extended printing durations and greater build volumes of the droplet-based printing system. Finally, to determine the system's lower resolution limits, we performed systematic downscaling of gyroid structures, testing dimensions ranging from the UV projector's nominal resolution to sub-resolution features. As shown in Fig. 2I, the downsized structure was fabricated by co-extruding 2 liquid resins at identical flow rates, resulting in the formation of a well-defined planar interface. Then, the side and bottom morphologies of the fabricated structures were systematically characterized (Fig. 2J to L and Fig. 2M to O, respectively). The measured structural resolution corresponds with the UV projector's nominal specifications. Remarkably, features as small as ~15 μm were achieved (Fig. 2O) along the printing direction, which can be attributable to the improved fabrication accuracy and stability afforded by the one-droplet 3D printing strategy [36].

Interfacial morphology control and multi-material construction

Building upon the demonstration of 2D multi-material patterned liquid as building slice with uninterrupted fabrication continuity, the extended capability for 3D material distribution control is further explored. Three distinct architectures were computationally designed to validate this approach: porous pumpkin-shaped structure featuring 2D planar interface (Fig. 3A), and 2 mushroom-shaped structures featuring fundamentally different 3D interfacial configurations (Fig. 3B and C). With real-time modulation of phase-specific extrusion parameters (Fig. 3D to F), precise fabrication of pumpkin-shaped structure maintaining perfect 2D interfacial planes (Fig. 3G) and mushroom-shaped structures with either continuous (Fig. 3J) or discontinuous (Fig. 3M) 3D interfaces can be bilateral extrusion printed. Multi-plane cross-sectional characterization (Fig. 3H and I, K and L, and N and O) reveals exceptional fidelity between as-printed and designed material distributions, confirming the reproducibility and spatial resolution of the bilateral extrusion platform.

By enabling simultaneous control over extruded material composition and number, the extension of this strategy in continuous 3D multi-material fabrication and its versatility in 3D control over material distribution and interfacial morphology are further investigated. For instance, by employing multi-delivery tubes and the regulation of extrusion number, distribution, and extruded material sequence, complex gyroid architectures can be realized with bimaterial systems featuring engineered planar and nonplanar interfaces, and multi-material variations with spatially programmed compositions in all 3 dimensions. In addition, Fig. 3P to R demonstrates excellent agreement between the fabricated 7-material structures and their digital models across all viewing angles, with precisely reproduced interfaces and material distributions matching the design specifications (Fig. 3S). Moreover, complex 3D material arrangements can be realized by layering structures featuring 2-material distributed block structures shown in Fig. 3T and U. Diverse 3D material configurations can be achieved by adjusting the stacking sequence, validating the capability to print 3D structures with user-defined material arrangement. As the core of this method employs patterned slices as molding unit, it is limited by the number of material and multi-material distribution complexity in current slice, material continuity during switching of different slices, and the increase or decrease in material species. The single-layer pattern is influenced by the pattern availability of the extrusion tube loading with different materials. Further, the requirement of interface boundary precision also influences the way of material switching and printing continuity. Based on different actual printing need, the extrusion device can be modified or corresponding auxiliary device can be added to further realize more flexible multi-material patterns along the current line.

Applications of CMAM approach

Leveraging precise control over material composition, spatial distribution, and interfacial morphology, we further demonstrate how this strategy enables advanced applications in anti-counterfeiting, shape-morphing structures, and soft robotics, which expands both the design possibilities and practical applications of 3D printing [62]. Extending beyond 2-material fabrication, this method enables single-process printing of 4-material pumpkin structures featuring control over surface exterior and internal composition distribution (Fig. S5 and Movie S3). Controlling the extrusion flow rates of the 4 kinds of materials, it is capable to fabricate multi-material pumpkin-shaped structures with identical exteriors (Fig. 4A to C) but differing internal distributions including nonuniform (Fig. 4D and E) or uniformly quaternary (Fig. 4F) distributions. Fluorescence microscopy clearly delineates all material interfaces, demonstrating both nonuniform (Fig. 4G) and uniform (Fig. 4J) 4-phase junctions, as well as dual 3-phase interfaces within individual structures (Fig. 4H and I). It should be

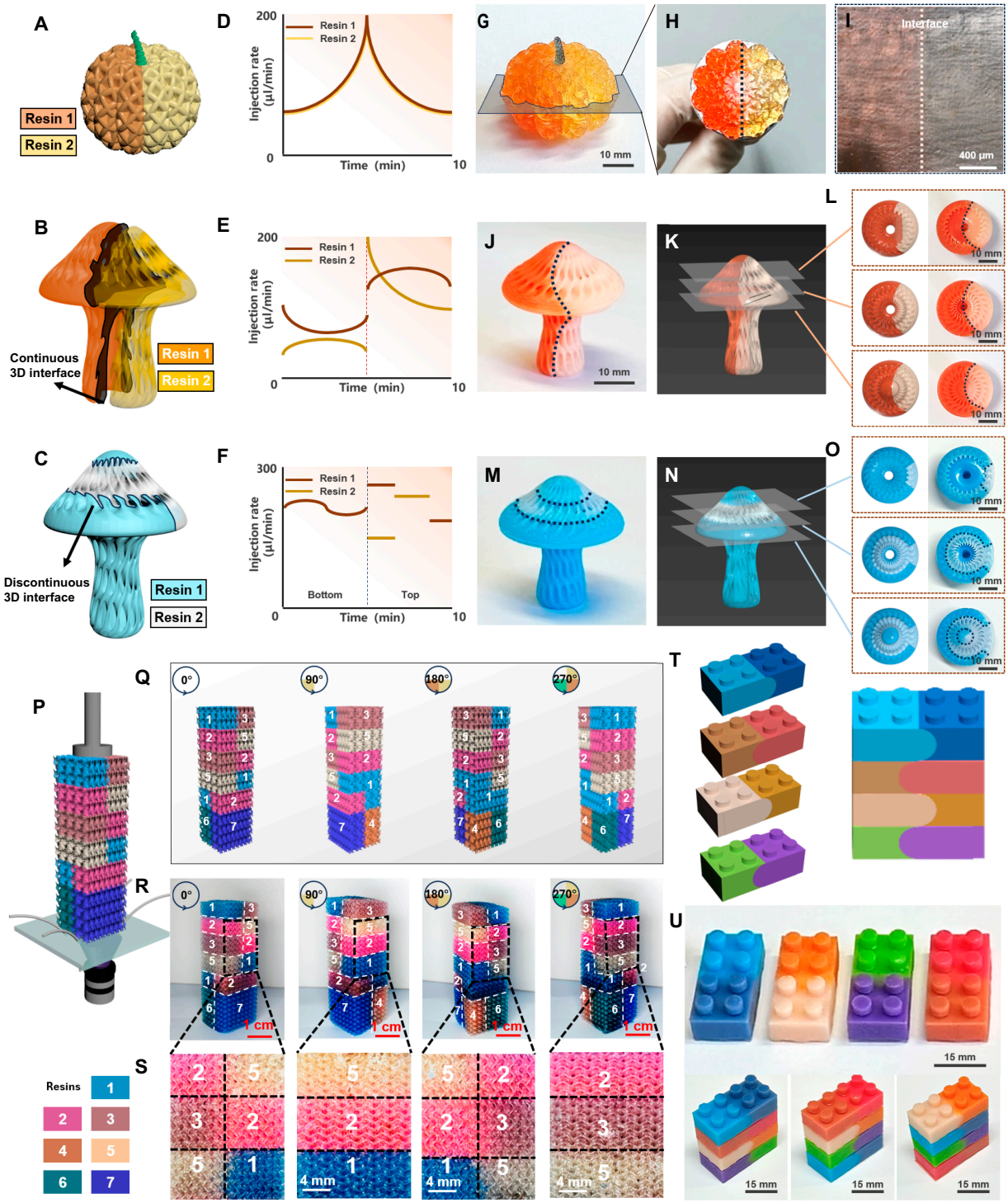


Fig. 3. Interfacial morphology control and continuous multi-material construction. (A) Digital 3D representation of the geometry of pumpkin-shaped structure. (B) Digital 3D representation of the geometry of mushroom-shaped structure featuring 3D continuous interface. (C) Digital 3D representation of the geometry of mushroom-shaped structure featuring 3D discontinuous interface. (D) Time-dependent extrusion rate profile for fabricating the pumpkin-shaped structure featuring inner 2D planar interface. (E) Time-dependent extrusion rate profile for fabricating mushroom-shaped structures featuring 3D continuous interfacial. (F) Time-dependent extrusion rate profile for fabricating mushroom-shaped structures featuring 3D discontinuous interface. (G) Optical characterization of the bilaterial extrusion-printed pumpkin-shaped structure. (H) Cross-sectional optical micrograph of the bilaterial extrusion-printed pumpkin-shaped structure. (I) High-magnification optical image of (H). (J) Optical characterization of the bilaterial extrusion-printed mushroom-shaped structure featuring 3D continuous interface. (K) Cross-sectional scheme of mushroom-shaped structure featuring 3D continuous interface. (L) Cross-sectional optical image interfaces in (K). (M) Optical characterization of the bilaterial extrusion-printed mushroom-shaped structure with 3D discontinuous interface. (N) Cross-sectional scheme mushroom-shaped structure featuring 3D discontinuous interface. (O) Cross-sectional optical image interfaces in (N). (P) Schematic diagram of the 7-color multi-material structure 3D representation and its construction configuration. (Q) Schematic diagram of the 7-color multi-material characterized from different directions. (R) Optical images of the printed 7-color multi-material 3D structure characterized from different directions. (S) Enlarged optical images in (R). (T) Schematic models of 4 block structures with different material distributions, and scheme of the stacking result. (U) Optical images of the bilaterial extrusion-printed 4 block structures with different material distributions, and experimental realization of material 3D distribution regulation by stacking the 4 block structures with different sequences.

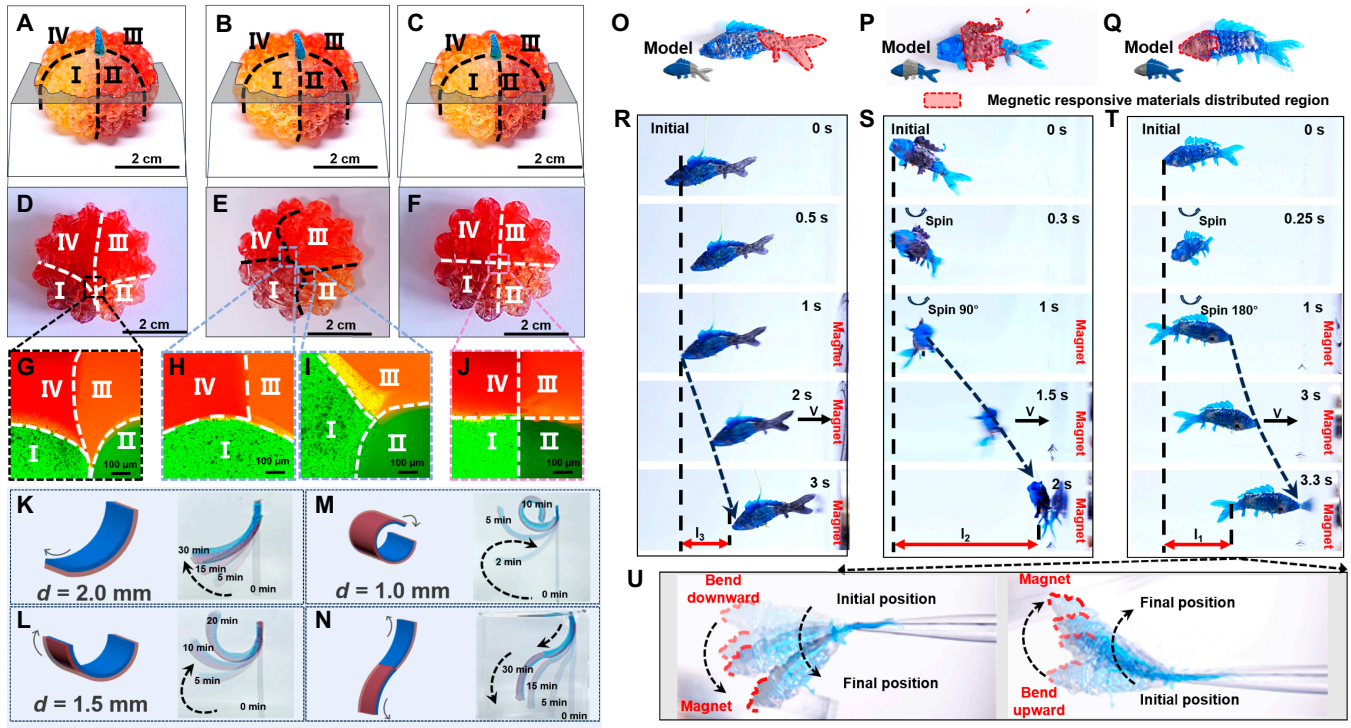


Fig. 4. Applications of CMAM approach. (A to F) Multi-material pumpkin-shaped structures exhibiting uniform exteriors with varied internal material arrangements. (A to C) Lateral optical images showing the surface characteristics of the pumpkin-shaped structures comprising 4 materials. (D to F) Cross-sectional optical images showing the internal distributions of the pumpkin-shaped structures comprising 4 materials featuring nonuniform (D and E) and uniformly quaternary (F) distributions. (D) to (F) display the corresponding cross-sectional views in (A) to (C), respectively. (G to J) Fluorescence images showing the internal distributions of the pumpkin-shaped structures comprising 4 materials featuring nonuniform (G) and uniformly quaternary (J) distributions, and the dual 3-phase interfaces within individual structures (H and J). (K to N) Schematic diagram and sequential optical micrographs showing the morphing evolution of multi-material structures fabricated via continuous bilateral extrusion. (K) Schematic diagram and time-lapse images showing the morphing evolution of a 2-mm-thick 2-material laminated structure (equal 1-mm phase thickness; 2 × 16 × 40 mm). (L) Schematic diagram and time-lapse images showing the morphing evolution of a 1.5-mm-thick 2-material laminated structure (equal 0.75-mm phase thickness; 1.5 × 16 × 40 mm). (M) Schematic diagram and time-lapse images showing the morphing evolution of a 1-mm-thick 2-material laminated structure (equal 0.5-mm phase thickness; 1 × 16 × 40 mm). (N) Schematic diagram and time-lapse images showing the morphing evolution of a 2-mm-thick 4-material laminated structure (equal 1-mm phase thickness; 2 × 16 × 40 mm). (O to Q) Scheme and optical characterization of 3D fish structures featuring magnetic-responsive materials at distinct anatomical positions: tail (O), abdomen (P), and head (Q). Schematics in (O) to (Q) illustrate the models of 3D fishes. (R to T) Sequential optical micrographs recording the dynamic behavior of fish constructs with regional magnetic responsiveness: (R) tail distribution, (S) abdomen distribution, and (T) head distribution during magnetic field application. (U) Magnetic field-induced head flexion in the fish featuring magnetic-responsive materials located at the head.

mentioned that the yellow region in Fig. 4I is due to the physical overlap of the structures, rather than fusion of the 2 materials, as displayed in Fig. S6. The nondestructive nature of these 4-material pumpkin structures conceals their internal distribution patterns, making them ideal for 3D printing anti-counterfeiting applications. This characteristic expands 3D printing's potential for creating complex 3D structures with precisely controlled material arrangements. While the present multi-material 3D printing process terminates upon completion of resin extrusion and UV projection, advancements can be achieved through system integration of machine learning-based optimization of extrusion system [51,63], through which real-time feedback control of extruded materials can be realized with improved system intelligence.

This strategy can also be extended in fabricating shape morphing structures by combining materials with distinct swelling properties, which is helpful for application in soft robotics. Upon immersion in anhydrous ethanol (Fig. S7), the asymmetric swelling behavior of the constituent materials induces curvature toward the component exhibiting lower volumetric expansion (Fig. 4K to N). By tuning the relative thickness of each side or the total thickness (d), the bending direction and magnitude are precisely controlled: Thinner structures exhibit faster curling speeds and greater deformation (Fig. 4K to N). Further control over bending morphology is achievable by increasing structural complexity through tailored material distribution and extrusion rates. For example, by designing a lamellar structure with opposing material arrangements in 2 sections, an S-shaped deformation is obtained upon swelling (Fig. 4N). Moreover, the method's high spatial material distribution control also enables printing of magnetic-responsive structures with programmable motion trajectories (Movie S4). For instance, 3D fish structures featuring regional magnetic responsiveness are bilateral extrusion printed through resins comprising flexible resin and Ni-loaded hard resin. Three fish structures with magnetic-responsive materials localized at the tail (Fig. 4O), abdomen (Fig. 4P), and head (Fig. 4Q) are designed and printed. Under a magnetic field, the tail-responsive fish moves directly toward the magnet (Fig. 4R), while the abdomen- and head-responsive variants first rotate 90° or 180°, respectively, before aligning to the magnet (Fig. 4S and T). Additionally, the head-responsive fish exhibits bending motion along with the magnet (Fig. 4U), highlighting the precision of this approach in governing 3D material arrangements and resultant functional behaviors.

Conclusion

In summary, this work demonstrates a continuous multi-material additive manufacturing (CMAM) strategy that simultaneously regulates solid–liquid and liquid–liquid interfacial properties. By preserving the droplet reservoir and receding TCL during UV curing, this approach eliminates volumetric construction constraints of one-droplet 3D printing while maintaining high material efficiency. Precise control over extrusion rates, material number, and spatial distribution enables the concurrent printing of 4 or more materials with programmable 2D (planar/curved) or 3D interfacial architectures. Furthermore, the application of fabricating anti-counterfeiting structures with spatially defined material distributions and 3D magnetic-responsive fish exhibiting programmable motion trajectories are realized, which expands the versatility and application scope of 3D printing. The proposed method provides unparalleled control in constructing intricate multi-material architectures, offering a transformative platform for continuous on-demand 3D fabrication of functional devices.

Materials and Methods

Commercial liquid resins from Formlabs (USA) including Elastic 50A resin, Castable wax 40 resin, Grey Pro resin v1, Clear resin, and Color kit resin (comprising a base resin and 5 color pigments) are employed. Specifically, Fig. 2's bimaterial structures with adjustable interfaces were printed from blue- and orange-loaded Clear resin. Mechanical test samples are fabricated from Clear resin (orange-dyed) and Castable Wax 40 resin. Multi-material characteristic structures utilized Color Kit resin to produce opaque matte parts in diverse colors. Shape-morphing structures are from Castable Wax 40 resin and red-dyed Elastic 50A resin. Rheology influenced fusion studies employed Elastic 50A resin, Castable wax 40 resin, Grey Pro resin v1, and Clear resin. Hard–Flexible–Hard structures for long-term interfacial mechanical testing were printed using pink-dyed Clear resin and Elastic 50A resin. The used resins in the same slice should be with the same curing volume under the same UV intensity.

Custom additive manufacturing system

The custom-designed additive manufacturing system comprised a 405-nm light-emitting diode (LED) UV projector (PRO6500S, Wintech, China, with projection area of 150 mm × 84 mm, resolution of 1,920 × 1,080 pixels, and adjustable intensity of 0 to 65 mW/cm^2), a liquid resin vat featuring a UV-transparent curing interface (quartz cell with perfluorocarbon-swollen polydimethylsiloxane-coated bottom), and an aluminum supporting plate (self-made) mounted on a programmable moving platform (MC600, Zolix Instruments Co. Ltd., China, offering translation speed of 1.5 to 100 mm/min) from bottom to up as displayed in Fig. 1A. The slicing thickness is set as 25 μm. All structures are printed under a printing speed of 3 mm/min.

Extrusion system

The extrusion setup comprises syringe pumps (LSP02-2B and dLSP520 Pro, Longer, China), injection syringes as resin container, and infusion tubes (1.5 mm diameter and 20 cm length) for resin delivery. The LSP02-2B syringe pump (dual-injection channels, linear velocity covering 5 μm/min to 130 mm/min, 140-mm maximum stroke with resolution of 0.156 μm/μstep) is used for resin extrusion for thermal phenomenon studies. The dLSP520 Pro syringe pump (dual-injection channels, linear velocity covering 0.04 μm/min to 86.4 mm/min, 108-mm maximum stroke with resolution of 0.015625 μm/μstep) is used for programmable resin extrusion in CMAM. During construction, the infusion tube and syringe are wrapped with tin paper to prevent liquid resin from exposure to light.

Post-processing for additive manufacturing

Following fabrication, absolute ethanol washing was performed until the rinse liquid appears clear to remove the residual ink on the printed structure and supporting plate. The sample is then detached from the support plate and subjected to post-curing in a UV LED chamber.

Characterization

Thermal imaging is characterized through an infrared camera (FLIR A655sc, USA) for real-time temperature dot or linear analysis. Process visualization is conducted through a digital camera (CU-VF100AC, JVC, Japan), through which optical images are captured for real-time monitoring of the construction process and structural evolution. Interface characterization is characterized using an optical microscope (BX53, OLYMPUS, Japan), scanning fluorescence microscope (FV1000-IX81, Olympus, Japan), and SEM (S-4800, Hitachi, Japan) at an accelerating voltage of 5.0 kV. Mechanical testing is realized through a digital load cell (M5-200, force threshold of 1,000 N, force resolution of 0.1 N, Mark-10 Corporation, USA) mounting on the programmable moving platform (ESM303, displacement resolution: 10.0 μm, Mark-10 Corporation, USA). Real-time force measurements were acquired synchronously with clamp displacement, enabling the construction of force–displacement profiles.

Acknowledgments

Funding: We acknowledge funding of the National Natural Science Foundation of China (grant no. 52173051), the Young Elite Scientist Sponsorship Program by CAST (2022QNRC001), and the Youth Innovation Promotion Association (2021031).
Author contributions: Conceptualization: L.W. Methodology: L.W. and J.S. Investigation: J.S. and W.X. Visualization: J.S., W.X., L.Z., and X.G. Supervision: L.W. and Y.L. Writing—original draft: J.S. and W.X. Writing—review and editing: W.L. Funding: L.W.
Competing interests: The authors declare that they have no competing interests.

Data Availability

All relevant data is present in the article and the Supplementary Materials.

Supplementary Materials

Figs. S1 to S7
Tables S1 to S3
Movies S1 to S4

References

1. Truby RL, Lewis JA. Printing soft matter in three dimensions. *Nature*. 2016;540(7633):371–378.

2. Zhang J, Bermingham MJ, Otte J, Liu Y, Hou Z, Yang N, Yin Y, Bayat M, Lin W, Huang X, et al. Ultrauniform, strong, and ductile 3D-printed titanium alloy through bifunctional alloy design. *Science*. 2024;383(6683):639–645.
3. Kuang X, Rong Q, Belal S, Vu T, López López AM, Wang N, Arıcan MO, Garciamendez-Mijares CE, Chen M, Yao J, et al. Self-enhancing sono-inks enable deep-penetration acoustic volumetric printing. *Science*. 2023;382(6675):1148–1155.
4. Kronenfeld JM, Rother L, Saccone MA, Dulay MT, DeSimone JM. Roll-to-roll, high-resolution 3D printing of shape-specific particles. *Nature*. 2024;627(8003):306–312.
5. Ritchie RO, Zheng XR. Growing designability in structural materials. *Nat Mater*. 2022;21(9):968–970.
6. Liu Z, Zhan Z, Shen T, Li N, Zhang C, Yu C, Li C, Si Y, Jiang L, Dong Z. Dual-bionic superwetting gears with liquid directional steering for oil-water separation. *Nat Commun*. 2023;14(1):4128.
7. Jung W, Jung YH, Pikhitsa PV, Feng J, Yang Y, Kim M, Tsai HY, Tanaka T, Shin J, Kim KY, et al. Three-dimensional nanoprinting via charged aerosol jets. *Nature*. 2021;592(7852):54–59.
8. Yuk H, Xu J, Luo J, Zhao X. 3D printing of conducting polymers. *Nat Commun*. 2020;11(1):1604.
9. Liu H, Zhang H, Han W, Lin H, Li R, Zhu J, Huang W. 3D printed flexible strain sensors: From printing to devices and signals. *Adv Mater*. 2021;33(8):Article 2004782.
10. Li JH, Cao J, Lu BY, Gu GY. 3D-printed PEDOT:PSS for soft robotics. *Nat Rev Mater*. 2023;8(9):604–622.
11. Duraivel S, Laurent D, Rajon DA, Scheutz GM, Shetty AM, Sumerlin BS, Banks SA, Bova FJ, Angelini TE. A silicone-based support material eliminates interfacial instabilities in 3D silicone printing. *Science*. 2023;379(6638):1248–1252.
12. Li D, Yang S, Zheng Z, Lai W-Y. Constructing lithium-free anode/separator interface via 3D carbon fabric scaffold for ultrasafe lithium metal batteries. *Research*. 2023;6:0267.
13. Sachyani Keneth E, Kamyshny A, Totaro M, Beccai L, Magdassi S. 3D printing materials for soft robotics. *Adv Mater*. 2020;33(19):2003387.
14. Wallin TJ, Pikul J, Shepherd RF. 3D printing of soft robotic systems. *Nat Rev Mater*. 2018;3(6):84–100.
15. Gladman AS, Matsumoto EA, Nuzzo RG, Mahadevan L, Lewis JA. Biomimetic 4D printing. *Nat Mater*. 2016;15(4):413–418.
16. Su RT, Park SH, Ouyang X, Ahn SI, McAlpine MC. 3D-printed flexible organic light-emitting diode displays. *Sci Adv*. 2022;8(1):Article eabl8798.
17. Lu Y, Zhang C, Xie T, Wu J. Grayscale color 3D/4D printing via orthogonal photochemistry. *Chem Bio Eng*. 2024;1(1):76–82.
18. Lee AR, Hudson AR, Shiwarski DJ, Tashman JW, Hinton TJ, Yerneni S, Bliley JM, Campbell PG, Feinberg AW. 3D bioprinting of collagen to rebuild components of the human heart. *Science*. 2019;365(6452):482–487.
19. Koffler J, Zhu W, Qu X, Platoshyn O, Dulin JN, Brock J, Graham L, Lu P, Sakamoto J, Marsala M, et al. Biomimetic 3D-printed scaffolds for spinal cord injury repair. *Nat Med*. 2019;25(2):263–269.
20. Wu SJ, Wu J, Kaser SJ, Roh H, Shiferaw RD, Yuk H, Zhao X. A 3D printable tissue adhesive. *Nat Commun*. 2024;15(1):1215.
21. Choi S, Lee KY, Kim SL, MacQueen LA, Chang H, Zimmerman JF, Jin Q, Peters MM, Ardoña HA, Liu X, et al. Fibre-infused gel scaffolds guide cardiomyocyte alignment in 3D-printed ventricles. *Nat Mater*. 2023;22(8):1036–1046.
22. Cheng L, Liu T, Liu Q, Lian L, Tang G, Mille LS, García FR, Engstrand L, Zhang YS, Du J. A 3D bioprinted gut anaerobic model for studying bacteria–host interactions. *Research*. 2023;6:0058.
23. Zheng X, Deotte J, Alonso MP, Farquar GR, Weisgraber TH, Gemberling S, Lee H, Fang N, Spadaccini CM. Design and optimization of a light-emitting diode projection micro-stereolithography three-dimensional manufacturing system. *Rev Sci Instrum*. 2013;83(12):Article 125001.
24. Sun C, Fang N, Wu DM, Zhang X. Projection micro-stereolithography using digital micro-mirror dynamic mask. *Sensor Actuat A Phys*. 2005;121(1):113–120.
25. Pan JA, Talapin DV. 3D-printing nanocrystals with light. *Science*. 2022;377(6610):1046–1047.
26. Ge Q, Chen Z, Cheng J, Zhang B, Zhang YF, Li H, He X, Yuan C, Liu J, Magdassi S, et al. 3D printing of highly stretchable hydrogel with diverse UV curable polymers. *Sci Adv*. 2021;7(2):Article eaba4261.
27. Wu L, Dong ZC. Interfacial regulation for 3D printing based on slice-based photopolymerization. *Adv Mater*. 2023;35(29):2300903.
28. De Beer MP, Van Der Laan HL, Cole MA, Whelan RJ, Burns MA, Scott TF. Rapid, continuous additive manufacturing by volumetric polymerization inhibition patterning. *Sci Adv*. 2019;5(1):Article eaau8732.
29. Machado TO, Stubbs CJ, Chiaradia V, Alraddadi MA, Brandolese A, Worch JC, Dove AP. A renewably sourced, circular photopolymer resin for additive manufacturing. *Nature*. 2024;629(8014):1069–1074.
30. Tumbleston JR, Shirvanyants D, Ermoshkin N, Janusziewicz R, Johnson AR, Kelly D, Chen K, Pinschmidt R, Rolland JP, Ermoshkin A, et al. Continuous liquid interface production of 3D objects. *Science*. 2015;347(6229):1349–1352.
31. Wu L, Dong Z, Du H, Li C, Fang NX, Song Y. Bioinspired ultra-low adhesive energy interface for continuous 3D printing: Reducing curing induced adhesion. *Research*. 2018;2018:Article 4795604.
32. Walker DA, Hedrick JL, Mirkin CA. Rapid, large-volume, thermally controlled 3D printing using a mobile liquid interface. *Science*. 2019;366(6463):360–364.
33. Regehly M, Garmshausen Y, Reuter M, König NF, Israel E, Kelly DP, Chou CY, Koch K, Asfari B, Hecht S. Xolography for linear volumetric 3D printing. *Nature*. 2020;588(7839):620–624.
34. Bertrand O, Gohy JF. Photo-responsive polymers: Synthesis and applications. *Polym Chem*. 2017;8(1):52–73.
35. Ligon SC, Liska R, Stampfl J, Gurr M, Mülhaupt R. Polymers for 3D printing and customized additive manufacturing. *Chem Rev*. 2017;117(15):10212–10290.
36. Zhang Y, Dong Z, Li C, Du H, Fang NX, Wu L, Song Y. Continuous 3D printing from one single droplet. *Nat Commun*. 2020;11:4685.
37. Wang M, Li W, Mille LS, Ching T, Luo Z, Tang G, Garciamendez CE, Lesha A, Hashimoto M, Zhang YS. Digital light processing based bioprinting with composable gradients. *Adv Mater*. 2022;34(1):2107038.
38. Liu SF, Hou ZW, Lin L, Li F, Zhao Y, Li XZ, Zhang H, Fang HH, Li Z, Sun HB. 3D nanoprinting of semiconductor quantum dots by photoexcitation-induced chemical bonding. *Science*. 2022;377(6610):1112–1116.
39. Zhang P, Lei IM, Chen G, Lin J, Liang X, Liu J, Chen X, Zhang J, Cai C, Liang X, et al. Integrated 3D printing of flexible electroluminescent devices and soft robots. *Nat Commun*. 2022;13:4775.

40. Liu WC, Chou VHY, Behera RP, Le Ferrand H. Magnetically assisted drop-on-demand 3D printing of microstructured multimaterial composites. *Nat Commun*. 2022;13(1):5150.
41. Cheng J, Wang R, Sun Z, Liu Q, He X, Li H, Ye H, Yang X, Wei X, Li Z, et al. Centrifugal multimaterial 3D printing of multifunctional heterogeneous objects. *Nat Commun*. 2022;13(1):7931.
42. Ouyang L, Armstrong JP, Lin Y, Wojciechowski JP, Lee-Reeves C, Hachim D, Zhou K, Burdick JA, Stevens MM. Expanding and optimizing 3D bioprinting capabilities using complementary network bioinks. *Sci Adv*. 2020;6(38):Article eabc5529.
43. Han D, Yang C, Fang NX, Lee H. Rapid multi-material 3D printing with projection micro-stereolithography using dynamic fluidic control. *Addit Manuf*. 2019;27:606–615.
44. Choi J-W, Kim H-C, Wicker R. Multi-material stereolithography. *J Mater Process Technol*. 2011;211(3):318–328.
45. Wang Z, Zhang B, He Q, Chen H, Wang J, Yao Y, Zhou N, Cui W. Multimaterial embedded 3D printing of composite reinforced soft actuators. *Research*. 2023;6:0122.
46. He CF, Qiao TH, Ren XC, Xie M, Gao Q, Xie CQ, Wang P, Sun Y, Yang H, He Y. Printability in multi-material projection-based 3-dimensional bioprinting. *Research*. 2025;8:0613.
47. Sun H, Zou B, Quan T, Wang X, Ma X, Xing H, Wei S, Huang C. Multi-material ceramic hybrid additive manufacturing based on vat photopolymerization and material extrusion compound process. *Addit Manuf*. 2025;97:Article 104627.
48. Jin J, Zhang F, Yang Y, Zhang C, Wu H, Xu Y, Chen Y. Hybrid multimaterial 3D printing using photocuring-while-dispensing. *Small*. 2023;19(50):2302405.
49. Skylar-Scott MA, Mueller J, Visser CW, Lewis JA. Voxelated soft matter via multimaterial multinozzle 3D printing. *Nature*. 2019;575(7782):330–335.
50. Peng X, Kuang X, Roach DJ, Wang Y, Hamel CM, Lu C, Qi HJ. Integrating digital light processing with direct ink writing for hybrid 3D printing of functional structures and devices. *Addit Manuf*. 2021;40:Article 101911.
51. Buchner TJ, Rogler S, Weirich S, Armati Y, Cangan BG, Ramos J, Twiddy ST, Marini DM, Weber A, Chen D, et al. Vision-controlled jetting for composite systems and robots. *Nature*. 2023;623(7987):522–530.
52. Narahara H, Tanaka F, Kishinami T, Igarashi S, Saito K. Reaction heat effects on initial linear shrinkage and deformation in stereolithography. *Rapid Prototyp J*. 1999;5(3):120–128.
53. Bauer J, Crook C, Baldacchini T. A sinterless, low-temperature route to 3D print nanoscale optical-grade glass. *Science*. 2023;380(6648):960–966.
54. Zhang Y, Wu L, Zou M, Zhang L, Song Y. Suppressing the step effect of 3D printing for constructing contact lenses. *Adv Mater*. 2021;34(4):2107249.
55. Larson NM, Mueller J, Chortos A, Davidson ZS, Clarke DR, Lewis JA. Rotational multimaterial printing of filaments with subvoxel control. *Nature*. 2023;613(7945):682–688.
56. Kuang MX, Wang LB, Song YL. Controllable printing droplets for high-resolution patterns. *Adv Mater*. 2014;26(40):6950–6958.
57. Li C, Cheng J, He Y, He X, Xu Z, Ge Q, Yang C. Polyelectrolyte elastomer-based ionotronic sensors with multi-mode sensing capabilities via multi-material 3D printing. *Nat Commun*. 2023;14(1):4853.
58. Li W, Liu J, Liu D, Li J, Wang J, Li J, Wang X, Su M, Li C, Song Y. Freely-shapable fabrication of aerogel patterns and 3D architectures by freeze-assisted transfer printing. *J Mater Chem C*. 2023;11(32):10834–10842.
59. Wehner M, Truby RL, Fitzgerald DJ, Mosadegh B, Whitesides GM, Lewis JA, Wood RJ. An integrated design and fabrication strategy for entirely soft, autonomous robots. *Nature*. 2016;536(7617):451–455.
60. Qu H, Gao C, Liu K, Fu H, Liu Z, Kouwer PH, Han Z, Ruan C. Gradient matters via filament diameter-adjustable 3D printing. *Nat Commun*. 2024;15(1):2930.
61. Ahn S-J, Lee H, Cho K-J. 3D printing with a 3D printed digital material filament for programming functional gradients. *Nat Commun*. 2024;15(1):3605.
62. Yan S, Zhang F, Luo L, Wang L, Liu Y, Leng J. Shape memory polymer composites: 4D printing, smart structures, and applications. *Research*. 2023;6:0234.
63. Brion DAJ, Pattinson SW. Generalisable 3D printing error detection and correction via multi-head neural networks. *Nat Commun*. 2022;13(1):4654.